Electronic Supplementary Material (ESI) for Chemical Communications.

Electronic Supplementary Information

Observation of uniform ligand environments and ^{31}P-^{197}Au coupling in phosphine-terminated Au nanoparticles

Lauren E. Marbella, Scott E. Crawford, Michael J. Hartmann and Jill E. Millstone*

Department of Chemistry, University of Pittsburgh, Pittsburgh, PA 15260, United States
Email: jem210@pitt.edu

Table of Contents:

Materials and Methods. 4-(diphenylphosphino)benzoic acid (4-DPPBA, 97%), bis(p-sulfonatophenyl)phenylphosphine dihydrate dipotassium salt (BSPP, 97%), hydrogen tetrachloroaurate(III) trihydrate ($HAuCl_4$, ≥ 99.9%), sodium borohydride ($NaBH_4$, ≥ 99.9%), chloro(triphenylphosphine)gold(I) (Au(I)Cl(PPh_3), ≥ 99.9%), acetic acid (glacial), and phosphoric acid solution (85% H_3PO_4) were purchased from Sigma Aldrich (St. Louis, MO). Deuterium oxide (99.9%) and methylene chloride-D_2 (D, 99.96%) were obtained from Cambridge Isotope Laboratories (Andover, MA). Sodium hydroxide (NaOH, ≥97% Certified ACS) was purchased from Fisher Scientific (Waltham, MA). All chemicals were used as received.

All aqueous solutions were prepared using NANOpure water (Thermo Scientific, > 18.2 MΩ·cm). 4-DPPBA was prepared in a 20.0 mM NaOH solution to ensure solubility of the DPPBA ligand. Prior to use, all glassware and Teflon-coated stir bars were washed with aqua regia (3:1 ratio of concentrated HCl to HNO_3) and rinsed with copious amounts of water prior to drying. *Caution: aqua regia is highly toxic and corrosive, and should only be used with proper personal protective equipment and training. Aqua regia should be handled only inside a fume hood.*

Synthesis of DPPBA-terminated gold nanoparticles. The synthesis of DPPBA-terminated gold nanoparticles has been described previously.[1] Briefly, 81.25 mL of water, 6.75 mL of a 10.0 mM 4-DPPBA solution, and 2.00 mL of a 20.0 mM $HAuCl_4$ solution were combined while stirring. After 20 s, 10.00 mL of a 20.0 mM $NaBH_4$ solution was rapidly injected, yielding a red-orange product. The solution was stirred for 1 min, and the particles were allowed to ripen for 1 h. Afterwards, the particles were centrifuged through 10 kDa molecular weight cut-off filters (Amicon Ultra – 4, Millipore, Inc) for 15 min at 4000 rcf (Eppendorf centrifuge 5804R with swing bucket rotor A-4-44). The particles were rinsed four additional times in a 3.30 mM NaOH solution (~ 4 mL). Following purification, the particles were analyzed using NMR spectroscopy, high resolution transmission electron microscopy (HRTEM), ultraviolet-visible-near infrared (UV-vis-NIR) spectroscopy, and X-ray photoelectron spectroscopy (XPS).

Solution phase ^{31}P NMR spectroscopy. DPPBA-terminated AuNPs were prepared for solution phase ^{31}P NMR spectroscopy by washing twice with 20 mM NaOH in D_2O, resuspending in 500 µL of 20 mM NaOH in D_2O, and loading the colloid into a 5 mm NMR tube. Other solutions that are discussed herein were prepared as follows: BSPP-terminated AuNPs were analyzed after following the same washing procedure as DPPBA-terminated AuNPs, with the exception that only NANOpure water and D_2O were used for particle resuspension and analysis. DPPBA alone in solution was recorded by preparing a 20 mM solution of DPPBA in 20 mM NaOH in D_2O. The ^{31}P NMR spectrum of Au(I)Cl(PPh_3) was recorded by preparing a 20 mM solution of Au(I)Cl(PPh_3) in CD_2Cl_2. Low temperature ^{31}P NMR measurements of DPPBA-terminated AuNPs were performed by resuspending lyophilized NP powders in CD_2Cl_2 and protonating via dropwise addition of glacial acetic acid.

All solution phase ^{31}P NMR experiments were recorded on a Bruker Avance III 600 MHz (14.1 T) spectrometer with a broadband fluorine observe (BBFO) Plus probe at 25°C, unless otherwise noted. Temperature was maintained using a Bruker BVT3000

variable temperature system. Low temperature ^{31}P NMR measurements were performed on a Bruker Avance III 400 MHz (9.4 T) spectrometer with a BBFO probe using nitrogen cooling to reach -25°C. ^{31}P chemical shifts were externally referenced to 85% H_3PO_4 (aq) at 0 ppm. Single pulse ^{31}P spectra were acquired after a π/2 pulse (typical pulse lengths ~11 μs) with WALTZ-16 ^{1}H decoupling during acquisition. Recycle delays varied for individual samples, but were maintained at $5\times T_1$, which ranged from ~10 s for DPPBA-terminated AuNPs to ~100 s for Au(I)Cl(PPh_3).

^{31}P diffusion ordered spectroscopy (DOSY) of DPPBA-terminated AuNPs and Au(I)Cl(PPh_3) were recorded using a stimulated echo sequence. The response of the ^{31}P NMR signal integration, *I*, to variation in gradient strength, *g*, is described by the Stejskal Tanner equation[2]:

$$\frac{I}{I_0} = exp\left(-g^2\gamma^2\delta^2\left(\Delta - \frac{\delta}{3}\right)\cdot D\right) \quad (1)$$

Where I_0 is the integral in the absence of gradients, γ is the gyromagnetic ratio of ^{31}P (108.29×10^6 rad/sT), δ is the length of the gradient pulse, and *D* is the measured diffusion coefficient. Although ^{31}P diffusion data is reported in the form of DOSY plots, it is important to note that all diffusion coefficients were extracted from linear fits of $\ln(I/I_0)$ data. In addition, rearrangement of the Stokes-Einstein equation was used to estimate the hydrodynamic size of the DPPBA-terminated AuNPs and Au(I)Cl(PPh_3) as follows:

$$r_H = \frac{k_B T}{6\pi\eta D} \quad (2)$$

Where r_H is the hydrodynamic radius, k_B is Boltzmann's constant, *T* is temperature, and η is solvent viscosity. A η value of 1.12 mPa·s for semi-heavy water, HDO, was used for the DPPBA-terminated AuNPs and 0.413 mPa·s for CD_2Cl_2. Reported errors were determined from the 2σ value extracted from the fit of the ^{31}P diffusion data.

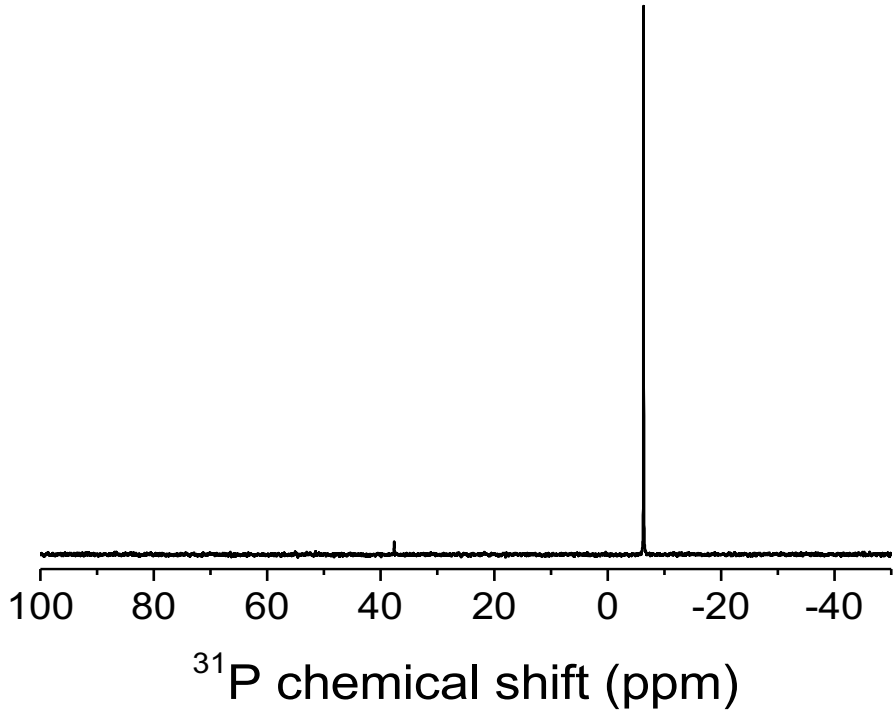

Figure S1. Solution phase ^{31}P NMR spectrum of 20 mM DPPBA (δ = -6.3 ppm) in 20 mM NaOH in D_2O at 14.1 T. The small peak at δ = +37.7 ppm was assigned to oxidized DPPBA, but only accounted for ~2 % of the total sample by signal integration.

Solid-state ^{31}P NMR spectroscopy. DPPBA-terminated AuNPs were prepared for solid-state ^{31}P NMR spectroscopy by lyophilizing nanoparticle solutions overnight. Dried nanoparticle powders and other solids (e.g. DPPBA, Au(I)Cl(PPh_3)) were packed into 4 mm zirconia rotors for analysis with ^{1}H-^{31}P cross-polarization magic-angle spinning (CPMAS) NMR. Prior to each sample analysis, the magic-angle was calibrated with KBr by maximizing the number of rotary echoes observed in the FID of ^{79}Br while spinning at 8 kHz. ^{1}H-^{31}P CPMAS NMR spectra were recorded on Bruker Avance 600 MHz (14.1 T) and Bruker Avance 500 MHz (11.7 T) spectrometers. Both were equipped with a triple-resonance 4 mm CPMAS probehead operating at a ^{31}P Larmor frequency of 243.11 MHz and 202.45 MHz and ^{1}H Larmor frequency of 600.57 MHz and 500.13 MHz, respectively. Temperature was maintained at 25°C with either a BCU05 (14.1 T) or BVT3000 (11.7 T) variable temperature unit, unless otherwise noted. ^{1}H-^{31}P Hartmann-Hahn match conditions were optimized using solid DPPBA. ^{1}H 90° pulse widths were ~4 μs at 14.1 T and ~5 μs at 11.7 T and contact times of 3 ms were used in both cases. Two-pulse phase-modulated (TPPM-20) high power ^{1}H decoupling at 80 kHz was applied during data acquisition. Typical MAS spinning rates between 5-12 kHz were used for all studies.

Recycle delays differed for individual samples, which depends on $T_{1H\rho}$, and varied from 3 s for DPPBA-terminated AuNPs to 500 s for Au(I)Cl(PPh_3).

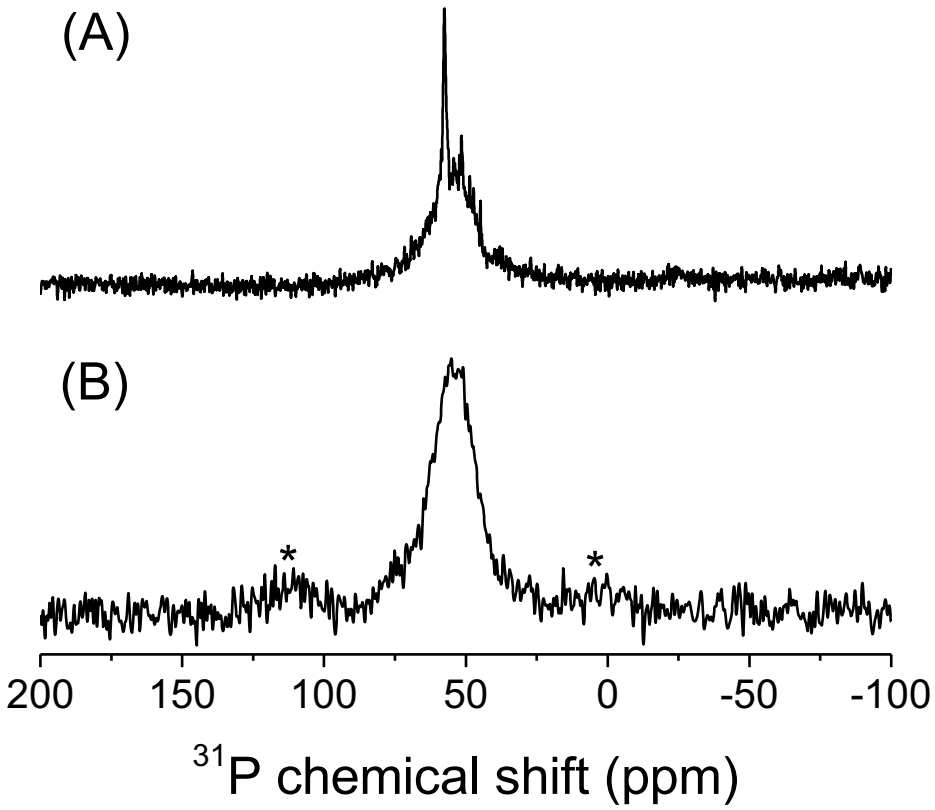

Figure S2. (A) Solution phase ^{31}P (δ sharp peak = +57.6 ppm) and (B) solid-state ^{1}H-^{31}P CPMAS (δ = +55.0 ppm) NMR spectra of BSPP-terminated AuNPs recorded at 14.1 T (A) and 11.7 T (B). Asterisks denote spinning sidebands, MAS = 10 kHz.

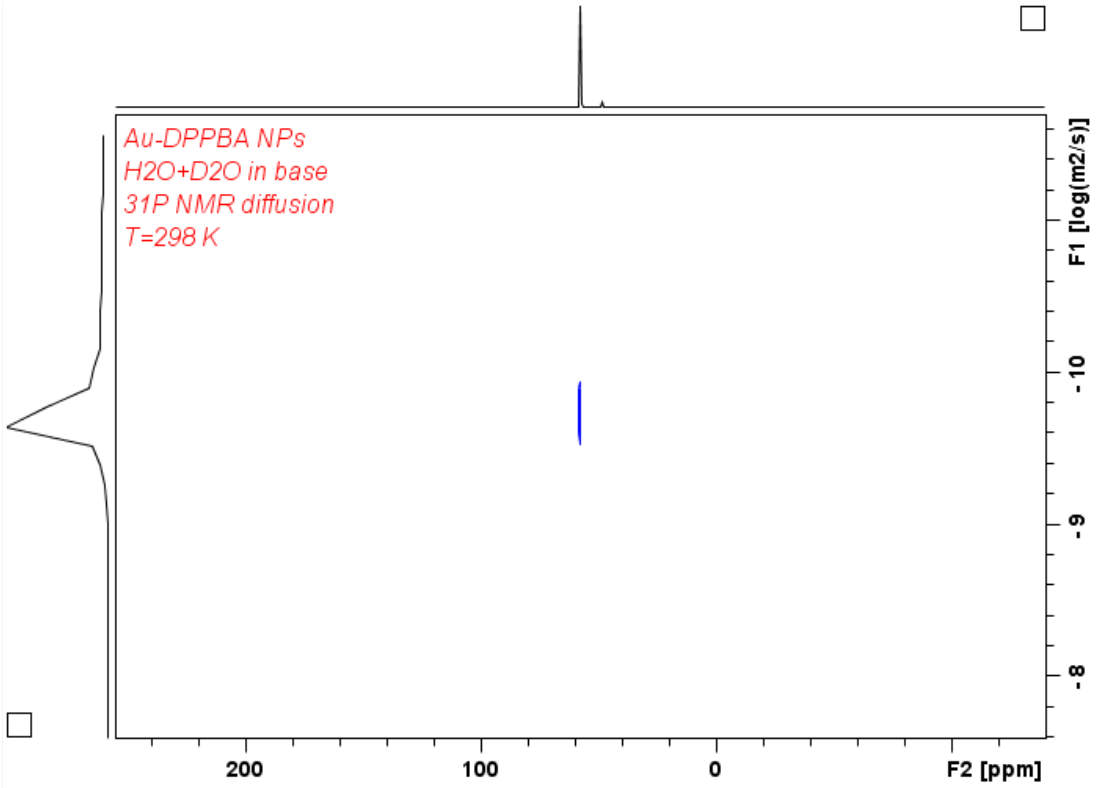

Figure S3. ^{31}P DOSY of DPPBA-terminated AuNPs recorded at 14.1 T at T = 25°C. Δ = 300 ms and δ = 5 ms.

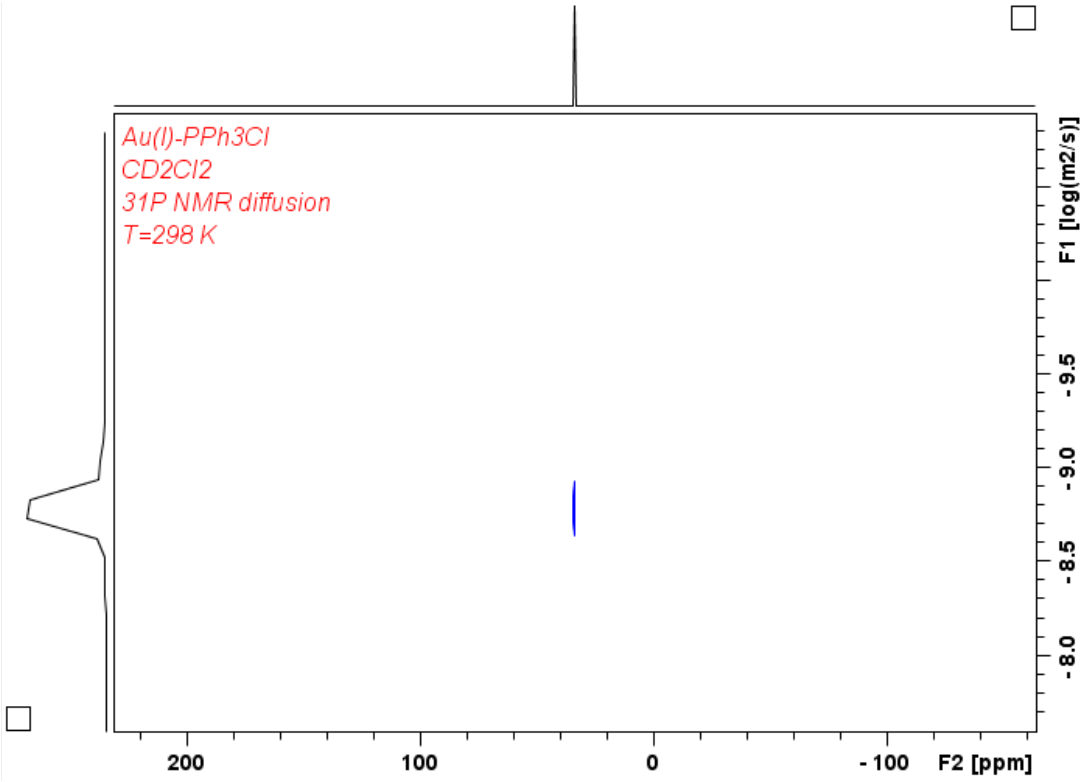

Figure S4. ^{31}P DOSY of Au(I)Cl(PPh_3) recorded at 14.1 T at T = 25°C. Δ = 125 ms and δ = 3 ms.

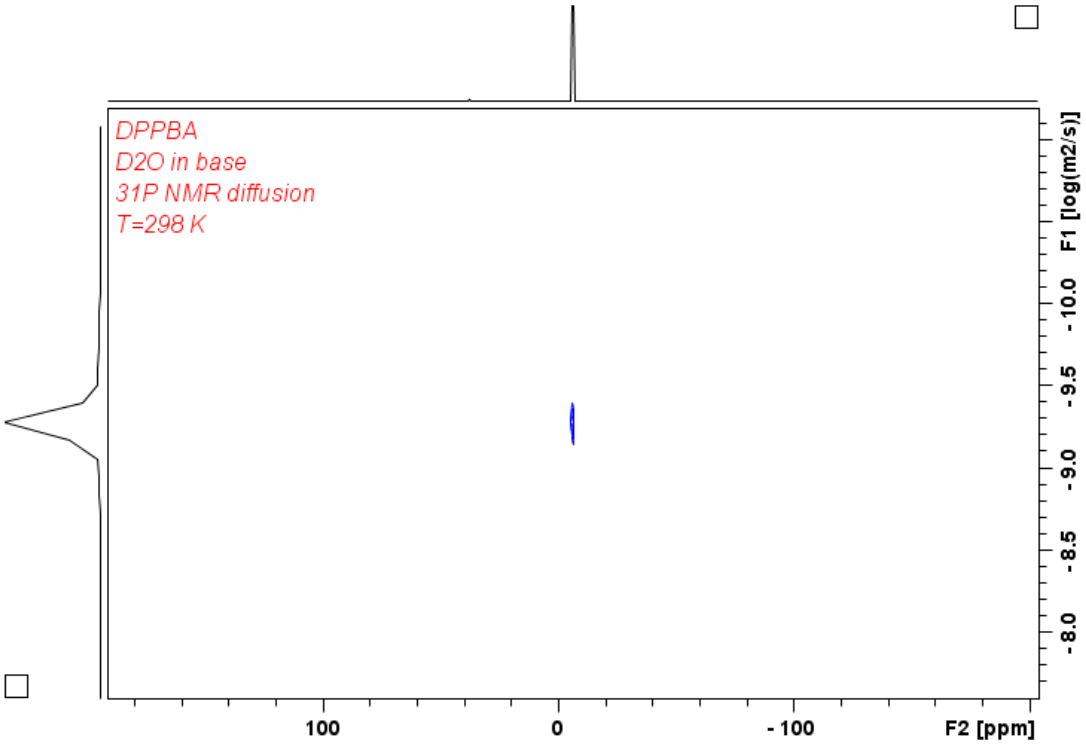

Figure S5. ^{31}P DOSY of DPPBA recorded at 14.1 T at T = 25°C. Δ = 125 ms and δ = 5 ms.

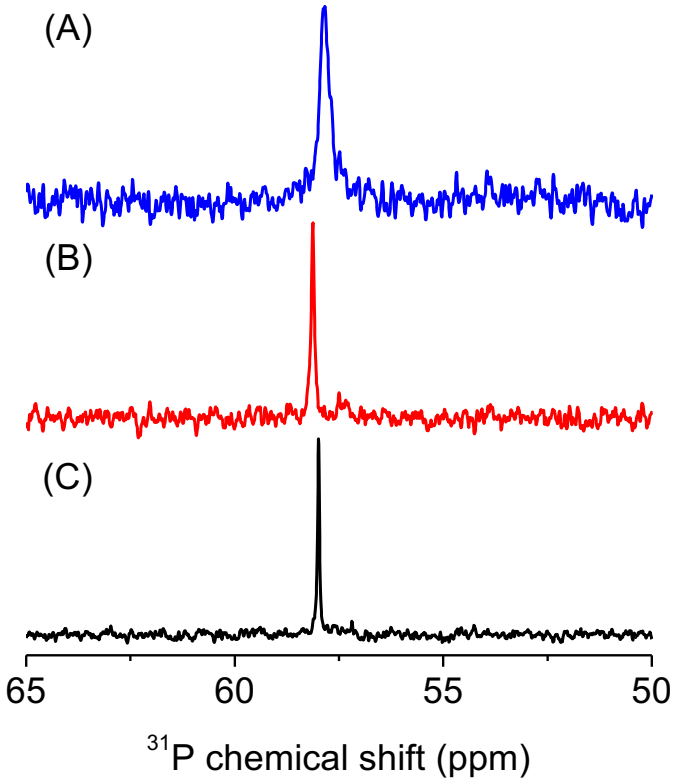

Figure S6. Solution ^{31}P NMR of DPPBA-terminated AuNPs in CD_2Cl_2 recorded at (A) -25°C, (B) 0°C, and (C) +25°C.

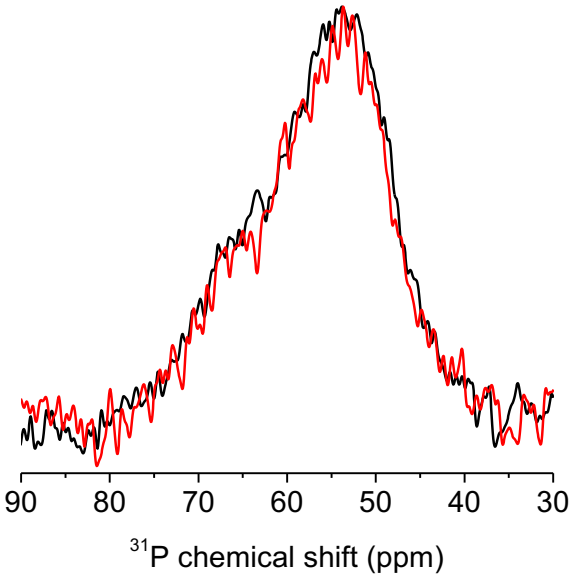

Figure S7. ^{1}H-^{31}P CPMAS NMR spectra of solid DPPBA-terminated AuNPs recorded at 25°C (black) and 62°C (red).

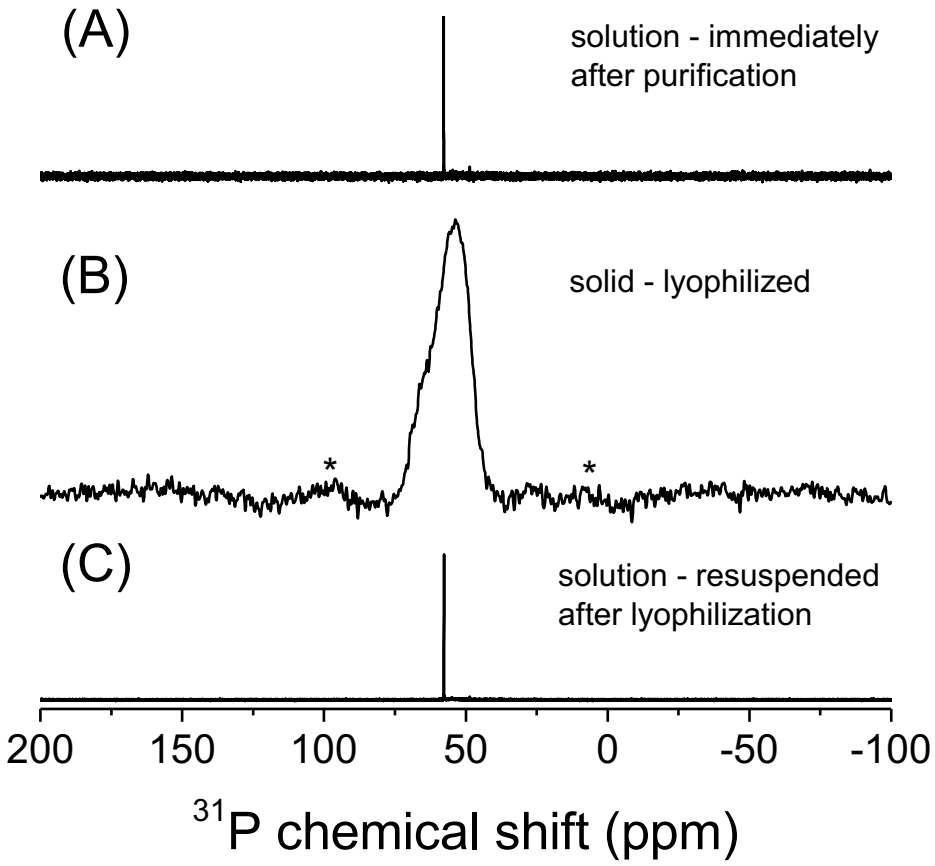

Figure S8. (A) Solution phase ^{31}P NMR of purified DPPBA-terminated AuNPs washed 4× with water and 2× with 20 mM NaOH in D_2O and diluted to volume in 20 mM NaOH in D_2O. (B) ^{1}H-^{31}P CPMAS NMR of purified, lyophilized DPPBA-terminated AuNP powders. MAS = 12 kHz. (C) Solution phase ^{31}P NMR of purified, lyophilized DPPBA-terminated AuNP powders that have been resuspended in 20 mM NaOH in D_2O. The peak position and fwhm in (C) is identical to that in (A). Higher SNR was achieved because the NP solutions were more concentrated after lyophilization and resuspension.

Ab initio calculations. Density functional theory (DFT) as implemented in the Amsterdam Density Functional (ADF) code was used to calculate electric field gradient (EFG) tensors, asymmetry parameters, and Euler angles.[3-5] EFG tensors were calculated with the hybrid B1LYP[6] exchange correlation functional with a polarized triple zeta basis set (TZ2P). This combination of functional and basis set has been shown to agree best with experimental results.[7] Relativistic effects for Au were accounted for within the Zeroth-Order Relativistic Approximation (ZORA).[8] In this report, four model systems were examined based on $Au_{11}(PPh_3)_7Cl_3$,[9] the two phosphorous binding sites in $[Au_{39}(PPh_3)_{14}Cl_6]Cl_2$,[10] as well as the single phosphorous binding motif in $Au_{55}(PPh_3)_{12}Cl_6$[11, 12] all shown in Figure S9. Calculated parameters used for inputs in spectral simulations are listed in Table S1.

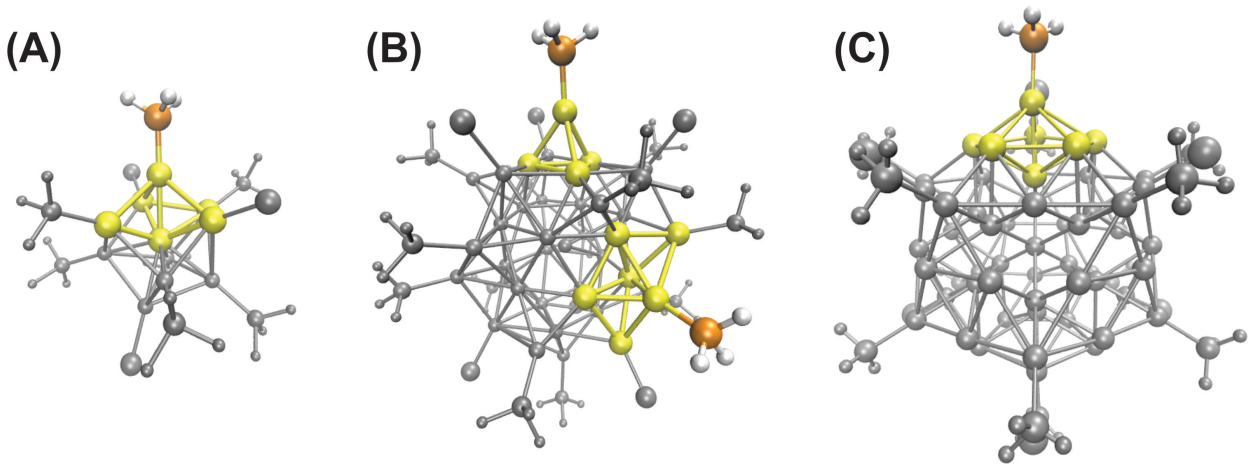

Figure S9. Crystal structures of (A) $Au_{11}(PPh_3)_7Cl_3$ from ref. 9, (B) $[Au_{39}(PPh_3)_{14}Cl_6]Cl_2$ from ref. 10, and (C) $Au_{55}(PPh_3)_{12}Cl_6$ from ref. 11. Orange = Au, Yellow = P, Green = Cl, Dark gray = C, White = H. Clusters are shaded in light gray for emphasis on ligand binding motifs. $[Au_{39}(PPh_3)_{14}Cl_6]Cl_2$ has two binding sites, one with C_1 symmetry and one with C_{3v} symmetry about the Au binding site.

Table S1. Nuclear properties of model phosphine binding motifs on AuNPs considered calculated with DFT.

Binding site	χ (MHz)	η	α^D (°)	β^D (°)
Au_{11}	-321.1	0.1996	127.1	5.6
Au_{39}-C_{3v}	-426.6	0.0998	74.5	177.5
Au_{39}-C_1	-279.5	0.2326	179.1	168.8
Au_{55}	287.5	0.3555	139.3	179.1

Quadrupole effects in ^{31}P ssNMR spectra. The line positions of spin-1/2 nuclei coupled to a quadrupolar nucleus can be described in terms of four parameters. When the spin-1/2 nucleus, I, is ^{31}P and the quadrupolar nucleus, S, is ^{197}Au, the relevant parameters are: (I) resonance frequency of the S nuclei, ^{197}Au (υ_s):

$$\upsilon_s = \gamma_{197Au} B_0 \quad (3)$$

The second, (II), is the ^{197}Au nuclear quadrupole coupling constant, χ:

$$\chi = \frac{e^2 qQ}{h} \quad (4)$$

where e is the electronic charge, q is the electric field gradient at the ^{197}Au nucleus, and Q is the quadrupole moment at the ^{197}Au nucleus. The Euler angles in Table S1 are defined as follows: β^D is the angle between the largest component of the EFG tensor and the internuclear vector, r_{IS}, and α^D is the azimuthal angle. The third relevant coupling constant, (III), is the ^{31}P-^{197}Au dipolar coupling constant, D:

$$D = (\mu_0/4\pi)(\gamma_{31P}\gamma_{197Au}/r_{IS}^3)(h/4\pi^2) \quad (5)$$

where r_{IS} is the internuclear vector based on P-Au bond length and μ_0 is the permeability of vacuum. Here, r_{IS} is 2.235 Å for Au(I)Cl(PPh_3)[13] and 2.29 Å for phosphine on a AuNP surface, based on the average bond length observed in $[Au_{39}(PPh_3)_{14}Cl_6]Cl_2$.[10] Based on these bond lengths, D = 75 Hz and 70 Hz for Au(I)Cl(PPh_3) and DPPBA-terminated AuNPs, respectively. The values for the ^{197}Au resonance frequency at 14.1 T and 11.7 T are 10.61 MHz and 8.84 MHz, respectively. In this case, χ is only known for Au(I)Cl(PPh_3) at 940 MHz,[14] but various possible values of χ were calculated with DFT and are considered for DPPBA-terminated AuNPs (*vide supra*, Table S1). Equation 5 represents the direct dipolar coupling, but the spectral features depend on the effective dipolar coupling constant, which is modulated by anisotropy (ΔJ) in the indirect spin-spin coupling constant tensor, as follows:

$$D_{eff} = D - \frac{\Delta J}{3} \quad (6)$$

Equation 6 assumes axial symmetry in the J-coupling tensor and that the J-coupling and direct dipolar coupling tensors are coincident with each other. For all simulations we assume that anisotropy is small and that ΔJ = 0. We note that large values of ΔJ and deviations from axial symmetry could dramatically change spectral features.

The final coupling constant, (IV), is the isotropic indirect spin-spin coupling constant, J_{iso}. Typical one bond J-couplings that have been observed for inorganic complexes range from $^1J(^{31}P\text{-}^{197}Au)$ = 120-700 Hz.[15, 16]

The form of the spin-1/2 spectrum depends on the ratio, R = D/J and on the dimensionless parameter K, which is defined as follows:

$$K = \frac{-3\chi}{4S(2S-1)Z} \quad (7)$$

We first consider the case of Au(I)Cl(PPh_3), since χ is known. For all values of D and J, R < 0.5, and the large value of χ = 940 MHz observed for Au(I)Cl(PPh_3), leading to large absolute values of |K| ≈ 23 and 28 at both 14.1 T and 11.7 T, respectively. Both R < 0.5 and the large absolute values of |K| require full diagonalization of the Hamiltonian for accurate spectral description, as outlined by Menger and Veeman.[21] At both field strengths studied, the $^1H\text{-}^{31}P$ CPMAS spectrum of Au(I)Cl(PPh_3) is predicted to collapse to the expected quartet to a doublet (Figure S10), and the spacing between the two observed lines is ~1.65 times the $^1J(^{197}Au\text{-}^{31}P)$ coupling constant. For smaller values of χ and consequently smaller values of |K|, we find that first-order perturbation theory may be sufficient to approximate $^1H\text{-}^{31}P$ CPMAS spectral lineshapes, especially in the case of partial self-decoupling (*vide infra*).

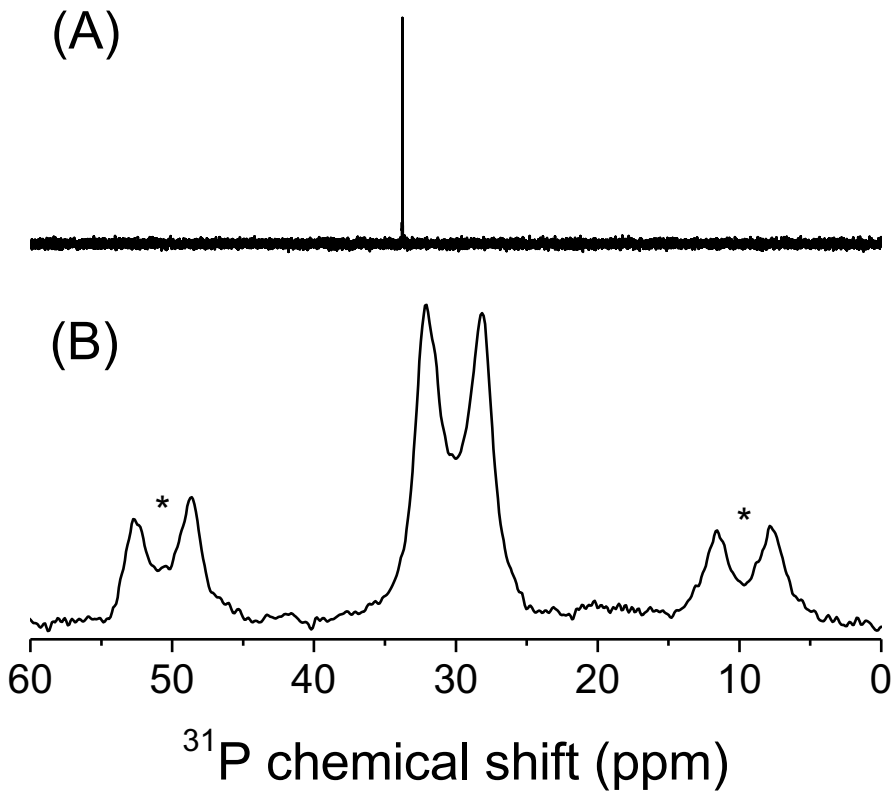

Figure S10. (A) Solution phase ^{31}P (δ = +33.8 ppm) and (B) solid-state ^{1}H-^{31}P CPMAS (δ = +30.2 ppm) NMR spectra of Au(I)Cl(PPh_3) recorded at 14.1 T. Asterisks denote spinning sidebands, MAS = 5 kHz.

^{31}P NMR Simulations. Spectral simulations were performed for both field strengths examined (14.1 T and 11.7 T) using the WSolids software.[22] For the DPPBA-capped AuNPs, we employed first-order perturbation theory, which has been used successfully to approximate spin-1/2 spectra of nuclei coupled to quadrupolar nuclei, even in cases when $\chi \geq \upsilon_s$.[23-25] The validity of using first-order perturbation theory to simulate the spectra of DPPBA-capped AuNPs was evaluated by comparing the spectral simulation of [Au(dppey)$_2$]I (dppey = cis-bis(diphenylphosphino)ethylene), for which the crystal structure and ^{1}H-^{31}P CPMAS has been reported.[26] Ab initio calculations showed that [Au(dppey)$_2$]I exhibited a χ value similar in magnitude to the particles (χ = -265 MHz). Using nuclear parameters from DFT, ^{31}P NMR spectra that resembled the experimental spectrum could be simulated with first-order perturbation theory.

In addition, quadrupolar nuclei that exhibit large χ values can exhibit fast quadrupolar T_1 relaxation. As a result of fast quadrupolar relaxation, the spin-1/2 spectrum may not exhibit the expected fine structure, and may be dramatically broadened,[27-29] due to partial self-decoupling. Since no distinct splittings were observed in our ^{31}P NMR spectra, the fast ^{197}Au T_1 relaxation was also taken into account in our simulations and the experimentally observed spectral breadth was simulated with line broadening in both the spectra of DPPBA-capped AuNPs and the ^{31}P NMR spectrum of Au(I)Cl(PPh_3) at both field strengths (Figures S11-S15).

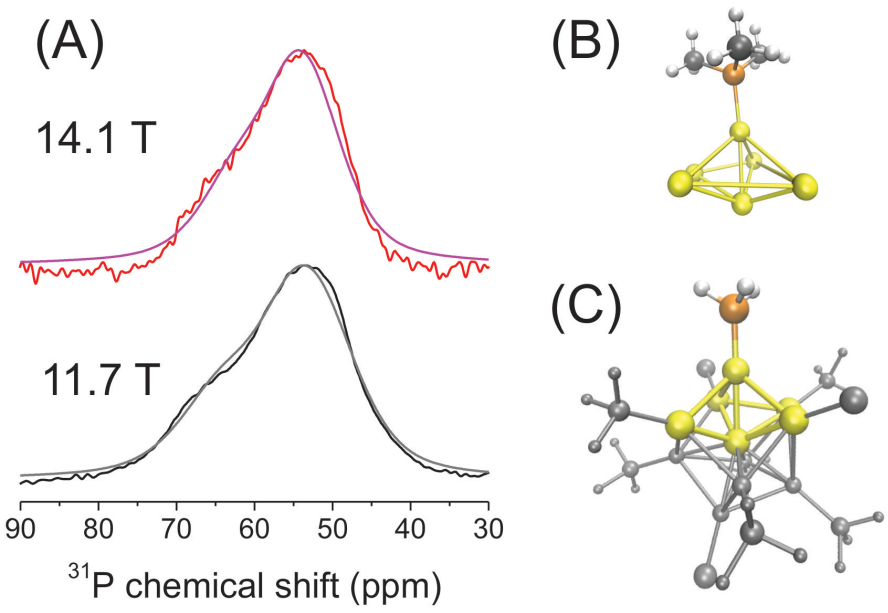

Figure S11. (A) Experimental ^{1}H-^{31}P CPMAS spectra of DPPBA-capped AuNPs (black, red) compared to simulated spectra (gray, purple) at 14.1 T (top) and 11.7 T (bottom) of (B) Au_{11} phosphine binding site. (C) Crystal structure of $Au_{11}(PPh_3)_7Cl_3$ from ref. 9 from which B was modeled. Simulation parameters = $^{1}J(^{31}P, ^{197}Au)$ = 650 Hz, LB = 2500 Hz.

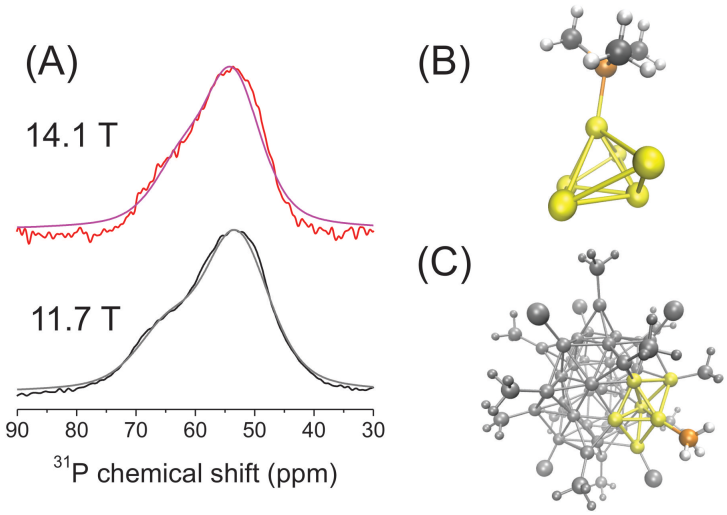

Figure S13. (A) Experimental ^{1}H-^{31}P CPMAS spectra of DPPBA-capped AuNPs (black, red) compared to simulated spectra (gray, purple) at 14.1 T (top) and 11.7 T (bottom) of (B) Au_{39} C_1 phosphine binding site. (C) Crystal structure of $[Au_{39}(PPh_3)_{14}Cl_6]Cl_2$ from ref. 10 from which B was modeled. Simulation parameters = $^{1}J(^{31}P, ^{197}Au)$ = 730 Hz, LB = 2500 Hz.

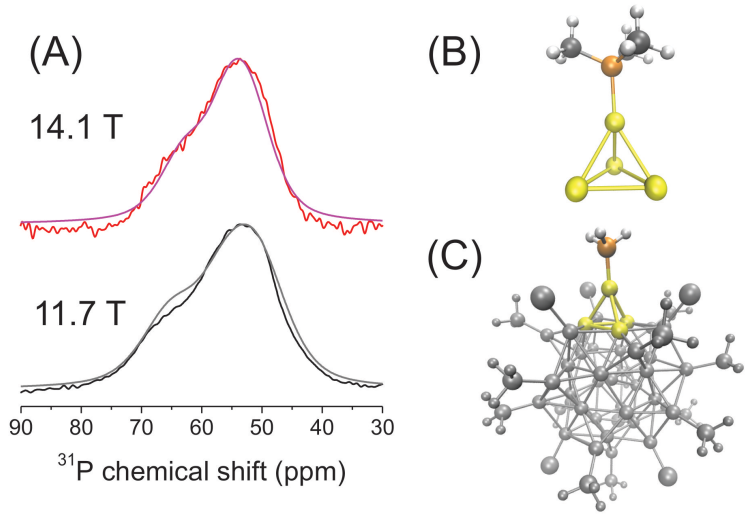

Figure S12. (A) Experimental ^{1}H-^{31}P CPMAS spectra of DPPBA-capped AuNPs (black, red) compared to simulated spectra (gray, purple) at 14.1 T (top) and 11.7 T (bottom) of (B) Au_{39} C_{3v} phosphine binding site. (C) Crystal structure of $[Au_{39}(PPh_3)_{14}Cl_6]Cl_2$ from ref. 10 from which B was modeled. Simulation parameters = $^{1}J(^{31}P, ^{197}Au)$ = 580 Hz, LB = 2500 Hz.

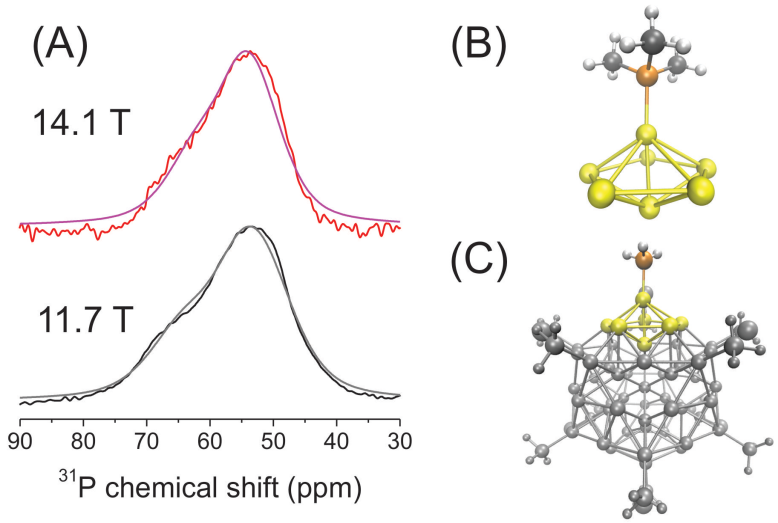

Figure S14. (A) Experimental ^{1}H-^{31}P CPMAS spectra of DPPBA-capped AuNPs (black, red) compared to simulated spectra (gray, purple) at 14.1 T (top) and 11.7 T (bottom) of (B) Au_{55} phosphine binding site. (C) Theoretical structure of $Au_{55}(PPh_3)_{12}Cl_6$ from which B was modeled. Simulation parameters = $^{1}J(^{31}P, ^{197}Au)$ = 650 Hz, LB = 2500 Hz.

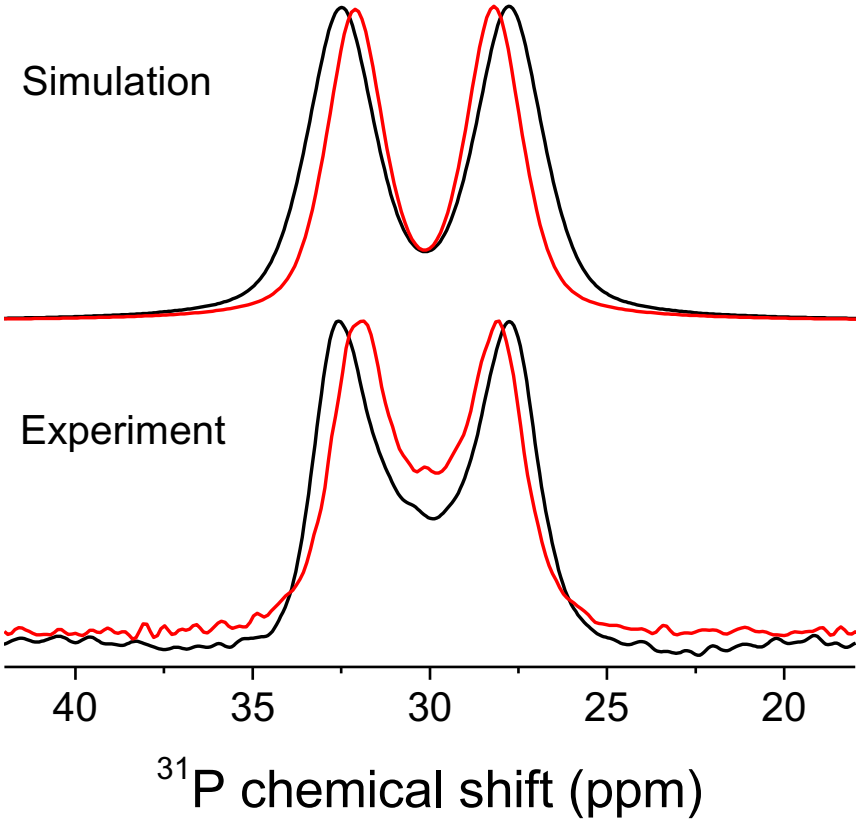

Figure S15. Experimental (bottom) and simulated (top) ^{1}H-^{31}P CPMAS spectra of Au(I)Cl(PPh_3) at 14.1 T (red) and 11.7 T (black). Simulation parameters = $^{1}J(^{31}P, ^{197}Au)$ = 575 Hz, LB = 450 Hz.

HRTEM. Purified DPPBA-terminated AuNPs were diluted 1:100 in water, and a 10.0 µL aliquot of the resulting solution was dropcast onto a lacey carbon TEM grid (Ted Pella, Inc.). Samples were allowed to air dry and were then dried under vacuum prior to characterization using a JEOL JEM 2100F operated at 200 kV and equipped with a Gatan Orius camera (Nanoscale Fabrication and Characterization Facility, Petersen Institute of Nanoscience and Engineering, University of Pittsburgh). The size distributions of AuNPs were determined from TEM images, and at least 200 individual AuNPs from various areas of the grid were measured. ImageJ 1.47d (National Institutes of Health, USA).[1]

Absorption spectroscopy. Purified DPPBA-terminated AuNPs in D_2O were characterized by ultraviolet-visible-near-infrared (UV-vis-NIR) absorption spectroscopy using a Cary 5000 spectrophotometer (Agilent, Inc.) using quartz cuvettes (Hellma, Inc.) with a 1 cm path length. All spectra were baseline corrected with respect to the spectrum of D_2O.

XPS. DPPBA-terminated AuNPs were dropcast directly from the purified colloidal solution in aqueous 20 mM NaOH onto clean (for ultra-high vacuum conditions)[30] 1 cm × 1 cm silicon (p-doped (boron)) wafers (University Wafer, Boston, MA). The wafers were allowed to air dry and then were placed under vacuum for at least 24 h prior to analysis with XPS. XPS was performed using an ESCALAB 250XI XPS with a monochromated, micro-focused Al Kα X-ray source (spot size = 400 μm). Survey and high resolution spectra were collected with a pass energy of 150 eV and 50 eV, respectively. Spectra were collected after Ar ion sputtering (500 eV, 10 seconds) prior to sample analysis. All XPS spectra were charge referenced to the adventitious carbon 1s peak at 284.8 eV.

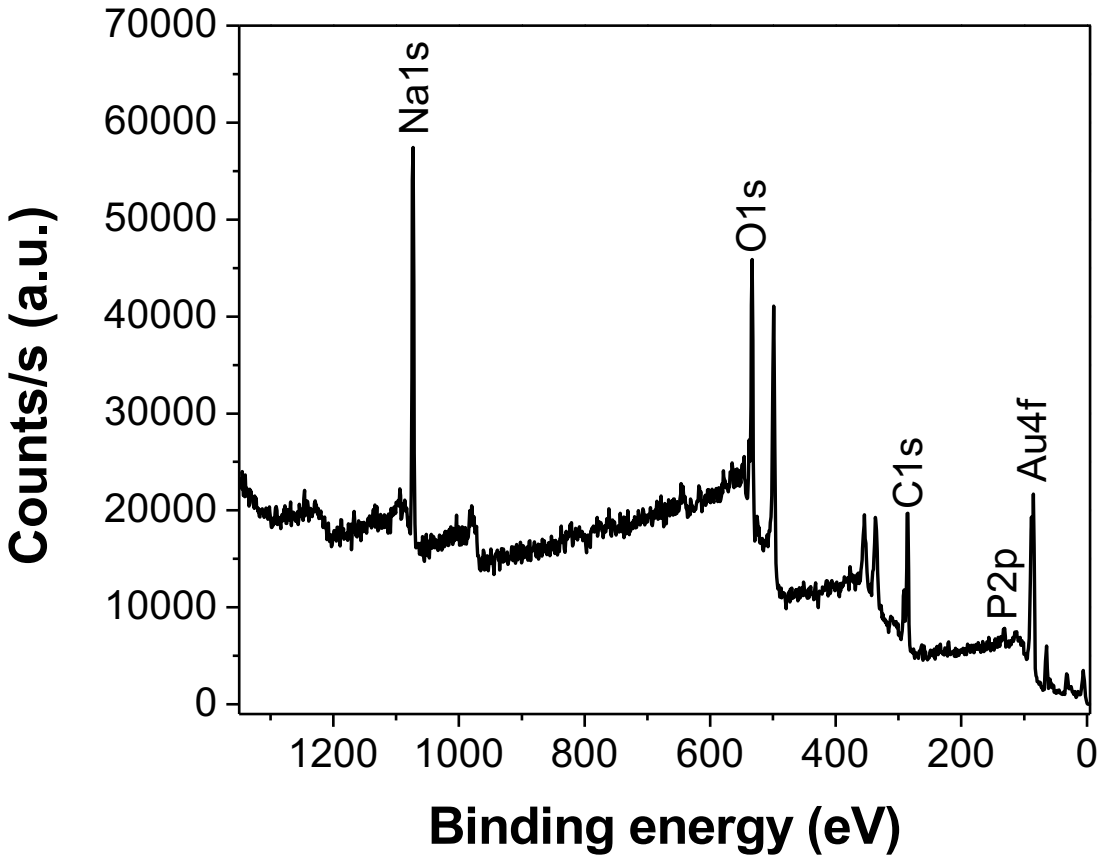

Figure S16. Survey XPS spectrum of DPPBA-terminated AuNPs.

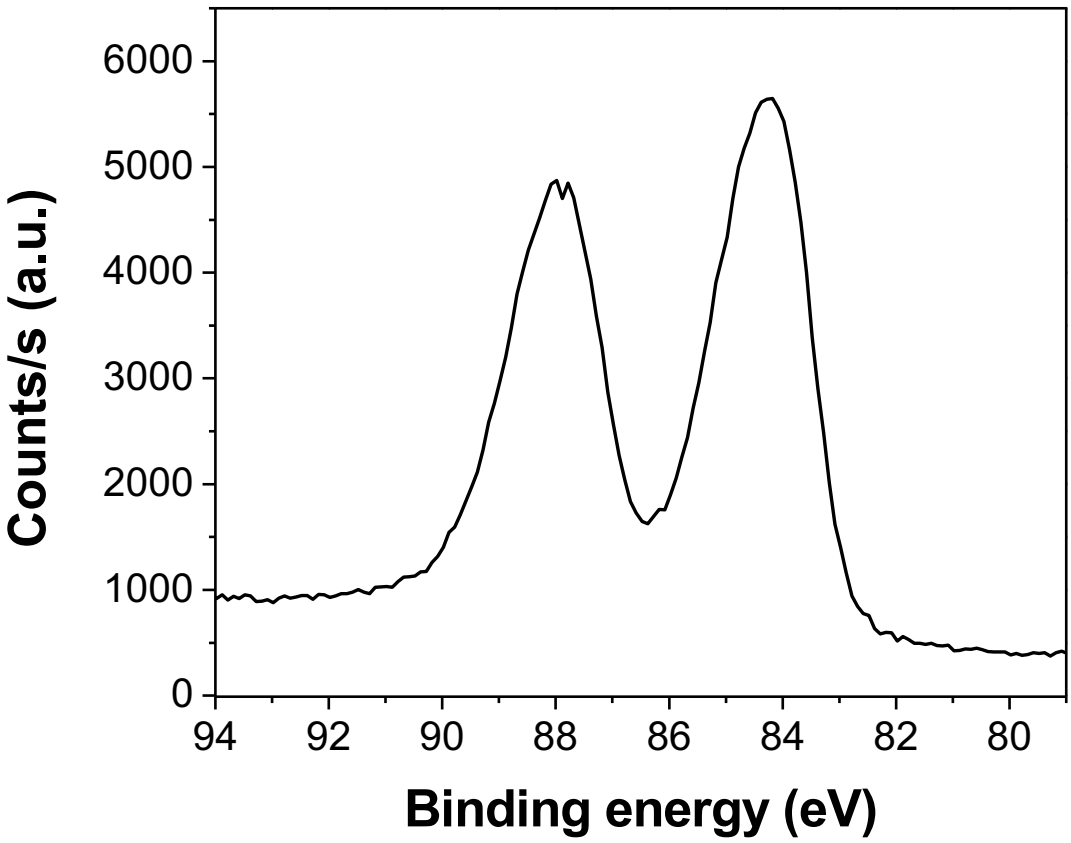

Figure S17. High resolution XPS of the Au4f region of DPPBA-terminated AuNPs.

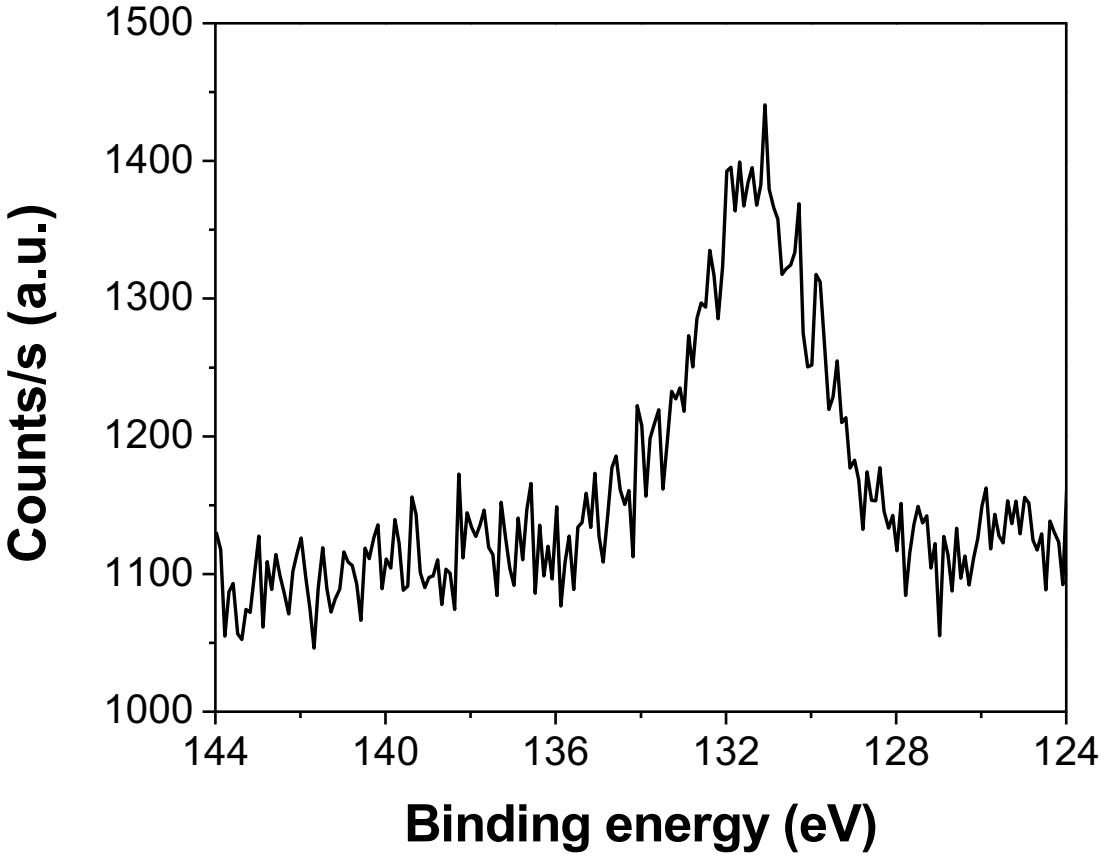

Figure S18. High resolution XPS of the P2p region of DPPBA-terminated AuNPs.

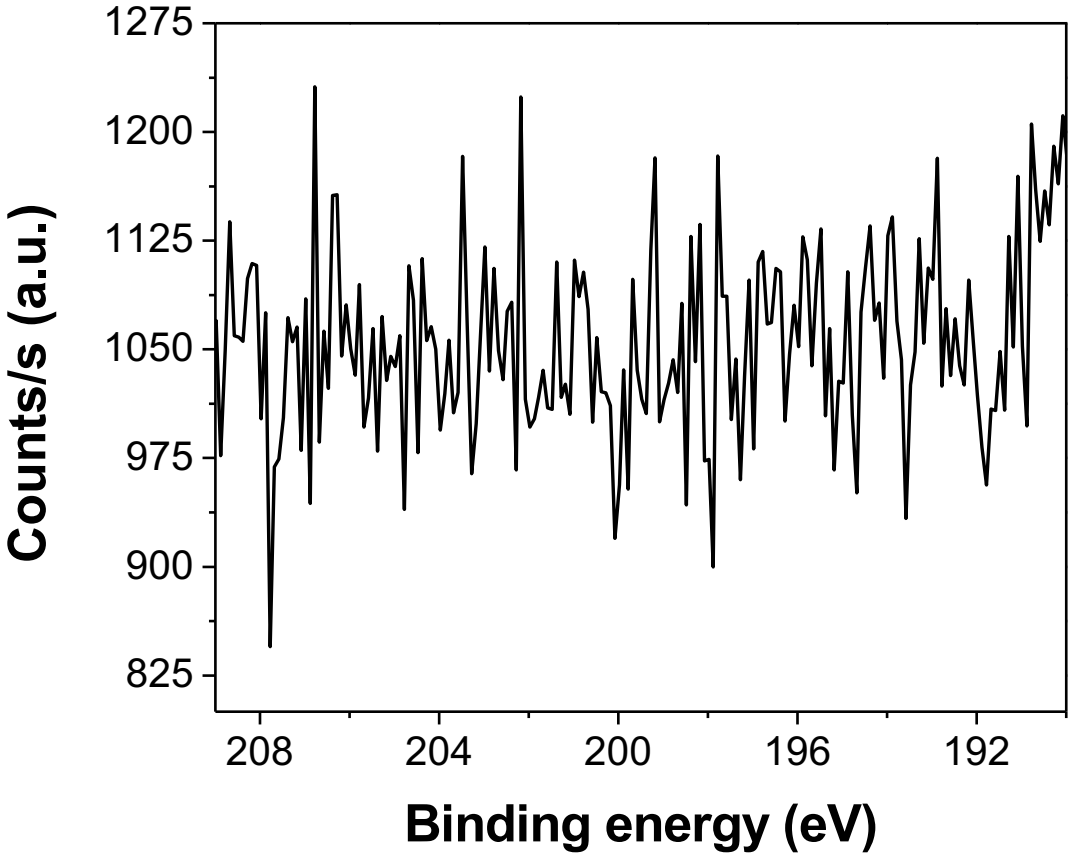

Figure S19. High resolution XPS of the Cl2p region of DPPBA-terminated AuNPs.

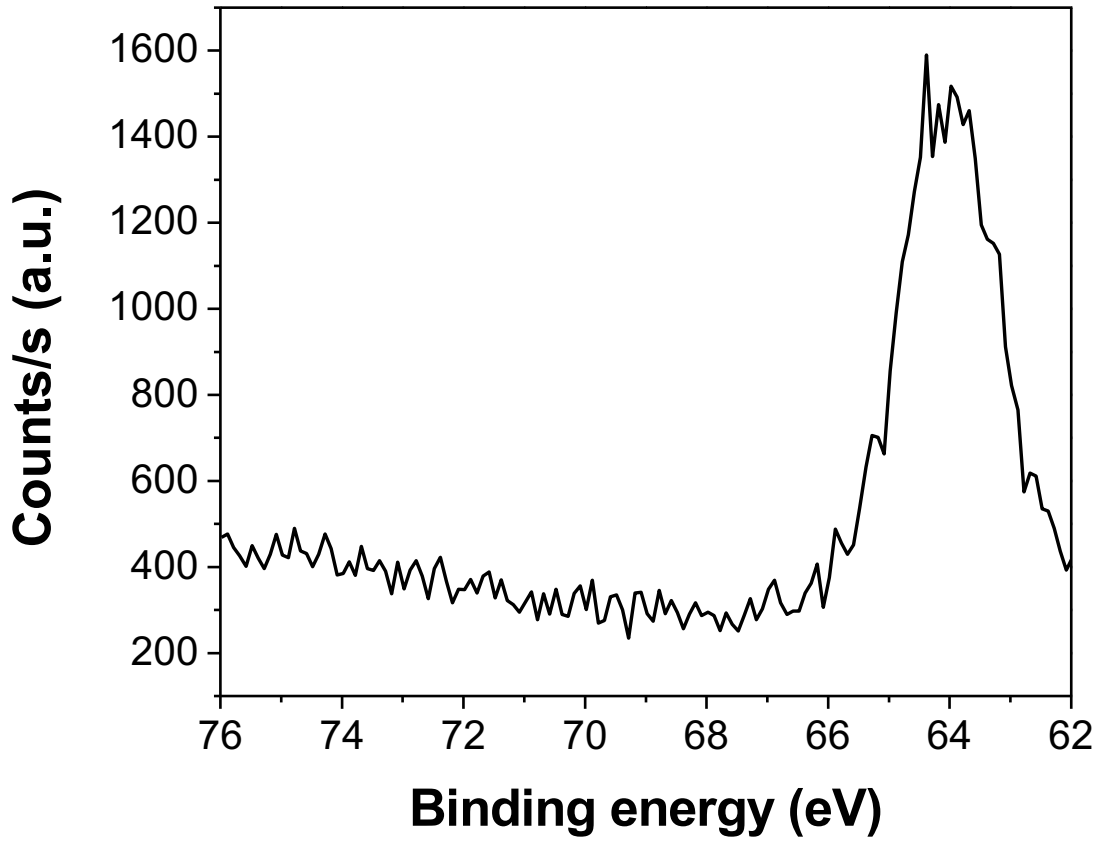

Figure S20. High resolution XPS of the Br3d region of DPPBA-terminated AuNPs. The peak observed at 64.1 eV is assigned to Na2s, which is present from the addition of NaOH to deprotonate the carboxylate on the capping ligand, and clearly observed in the survey spectrum (Figure S16). Br bound to a metal exhibits a chemical shift at ~69 eV.

References:

1. S. E. Crawford, C. M. Andolina, A. M. Smith, L. E. Marbella, K. A. Johnston, P. J. Straney, M. J. Hartmann and J. E. Millstone, *J. Am. Chem. Soc.*, 2015, **137**, 14423-14429.
2. E. O. Stejskal and J. E. Tanner, *J. Chem. Phys.*, 1965, **42**, 288-292.
3. J. Autschbach, S. Zheng and R. W. Schurko, *Concept Magn. Res. A*, 2010, **36A**, 84-126.
4. J. Autschbach and T. Ziegler, *J. Chem. Phys.*, 2000, **113**, 9410-9418.
5. G. te Velde, F. M. Bickelhaupt, E. J. Baerends, C. Fonseca Guerra, S. J. A. van Gisbergen, J. G. Snijders and T. Ziegler, *J. Comput. Chem.*, 2001, **22**, 931-967.
6. C. Adamo and V. Barone, *Chem. Phys. Lett.*, 1997, **274**, 242-250.
7. J. R. Dwan, Masters Thesis, University of Alberta, 2011.

8. E. v. Lenthe, E. J. Baerends and J. G. Snijders, *J. Chem. Phys.*, 1993, **99**, 4597-4610.
9. L. C. McKenzie, T. O. Zaikova and J. E. Hutchison, *J. Am. Chem. Soc.*, 2014, **136**, 13426-13435.
10. B. K. Teo, X. Shi and H. Zhang, *J. Am. Chem. Soc.*, 1992, **114**, 2743-2745.
11. Y. Pei, N. Shao, Y. Gao and X. C. Zeng, *ACS Nano*, 2010, **4**, 2009-2020.
12. G. Schmid, R. Pfeil, R. Boese, F. Bandermann, S. Meyer, G. H. M. Calis and J. W. A. van der Velden, *Chem. Ber.*, 1981, **114**, 3634-3642.
13. N. C. Baenziger, W. E. Bennett and D. M. Soborofe, *Acta Crystallogr. Sect. B*, 1976, **32**, 962-963.
14. P. G. Jones, A. G. Maddock, M. J. Mays, M. M. Muir and A. F. Williams, *J. Chem. Soc., Dalton Trans.*, 1977, 1434-1439.
15. L.-J. Baker, G. A. Bowmaker, P. C. Healy, B. W. Skelton and A. H. White, *J. Chem. Soc., Dalton Trans.*, 1992, 989-997.
16. S. J. Berners-Price, L. A. Colquhoun, P. C. Healy, K. A. Byriel and J. V. Hanna, *J. Chem. Soc., Dalton Trans.*, 1992, 3357-3363.
17. D. C. Apperley, B. Haiping and R. K. Harris, *Mol. Phys.*, 1989, **68**, 1277-1286.
18. A. C. Olivieri, *J. Magn. Reson.*, 1989, **81**, 201-205.
19. A. C. Olivieri, *Magn. Reson. Chem.*, 1996, **34**, 365-367.
20. A. C. Olivieri, L. Frydman and L. E. Diaz, *J. Magn. Reson.*, 1987, **75**, 50-62.
21. E. M. Menger and W. S. Veeman, *J. Magn. Reson.*, 1982, **46**, 257-268.
22. K. Eichele, WSolids1, version 1.21.3, Universität Tübingen, Tübingen, Germany, 2015.
23. S. H. Alarcón, A. C. Olivieri and R. K. Harris, *Solid State Nucl. Magn. Reson.*, 1993, **2**, 325-334.
24. J. G. Hexem, M. H. Frey and S. J. Opella, *J. Chem. Phys.*, 1982, **77**, 3847-3856.
25. A. C. Olivieri, *J. Magn. Reson. A*, 1993, **101**, 313-316.
26. P. C. Healy, B. T. Loughrey, G. A. Bowmaker and J. V. Hanna, *Dalton Trans.*, 2008, 3723-3728.
27. R. W. Schurko, R. E. Wasylishen and J. H. Nelson, *J. Phys. Chem.*, 1996, **100**, 8057-8060.
28. G. Szalontai, in *Current Developments in Solid State NMR Spectroscopy*, eds. N. Müller and P. Madhu, Springer Vienna, 2003, ch. 6, pp. 95-106.
29. H. Yu, X. Tan, G. M. Bernard, V. V. Terskikh, J. Chen and R. E. Wasylishen, *J. Phys. Chem. A*, 2015, **119**, 8279-8293.
30. P. J. Straney, C. M. Andolina and J. E. Millstone, *Isr. J. Chem.*, 2015, DOI: 10.1002/ijch.201500033.